

Enhanced Electron Transport in Heterojunction Sn-Perovskite Solar Cells Assisted by [6,6]-Phenyl-C61-butyric Acid Methyl Ester as a Dopant

Ajay Kumar Baranwal,*# Huan Bi,[#] Gaurav Kapil, Takeshi Kitamura, Liang Wang, Jiaqi Liu, Qing Shen, and Shuzi Hayase*



Cite This: *ACS Energy Lett.* 2024, 9, 4119–4126



Read Online

ACCESS |

Metrics & More

Article Recommendations

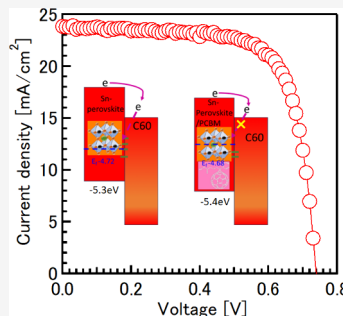
Supporting Information

ABSTRACT: Tin halide perovskite (THP) possesses p-type semiconducting properties owing to innate Sn oxidative defect states. These defect states create imbalance in charge collection at the interfaces, which hinders overall solar cell efficiency. To effectively harness THP's potential, we introduced a strategic n-type commonly used material, [6,6]-phenyl-C61-butyric acid methyl ester (PCBM), as a dopant, which has rarely been discussed. The coupling of PCBM and THP, validated through experimental and density functional theory methods, effectively targeted Sn defect states and transformed the THP semiconducting nature from p-type to intrinsic. Furthermore, strategically positioned PCBM at the grain boundaries offered multiple benefits, including improved adhesion between grains, leading to reduced lattice strain, enhanced energetic matching, and efficient charge transfer. This positng effectively harnessed electron collection due to PCBM's n-type electronic properties, leading to an enhanced PCE. This blend strategy, broadly followed in organic solar cells, led to the development of PCBM-THP heterojunction solar cells, achieving a record efficiency of 12.68%.

The rapid advancement of Pb-perovskite solar cells has positioned them as one of the fastest-growing technologies within the solar cell industry. However, concerns regarding the toxicity of Pb have driven extensive exploration into Pb-free alternatives.¹ Among these alternatives, Sn-halide perovskite (THP) solar cells have shown remarkable progress in photoconversion efficiency (PCE) and stability over the years.² This advancement can be attributed to the exceptional optoelectronic properties of THPs, which include a suitable narrow band gap, strong light absorption coefficient, low exciton binding energy, high carrier mobility, efficient photoluminescence, and suppressed ion migration.^{1–5}

Initially, THP solar cells designed with a regular structure achieved around 6% PCE.⁶ However, performance was limited by electron extraction at the defect-prone metal-oxide electron transport layer, leading to the formation of Sn vacancies and defects.^{7,8} This limitation became a barrier to further advancements.² Subsequently, attention shifted to an inverted structure, wherein THP inks were coated onto an organic poly(3,4-ethylenedioxythiophene)-poly(styrenesulfonate) (PEDOT:PSS) layer. Despite this change, challenges in THP solar cell performance remained due to rapid THP crystallization and vulnerability to oxidation. To address these issues, SnF₂ was used as a dopant to slow down the crystallization and

compensate Sn vacancies.⁹ Simultaneously, thin SnS formed over PEDOT:PSS acted as a protective layer to reduce charge recombination.¹⁰ Since then, various strategies have been explored to enhance THP solar cell performance, including solvent engineering,^{11–13} surface passivation,^{14–16} substitution/additive engineering,^{17–21} and heterogeneous engineering.^{22–24} These strategies collectively mitigate tin vacancies and background current density by controlling the crystallization process. The oxidative effects of cosolvent dimethyl sulfoxide (DMSO)²⁵ were mitigated by adjusting the THP precursor stirring protocol and incorporating GeI₂ as an additive.¹¹ This resulted in the formation of a protective GeO_x layer, further shielding the surface against moisture intrusion.²⁶ Interfacial defects were successfully passivated using guanidium with a cocation strategy.²⁷ Further improvements came from a triple cation strategy involving cesium and imidazolium which

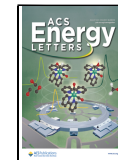


Received: June 17, 2024

Revised: July 19, 2024

Accepted: July 24, 2024

Published: July 29, 2024



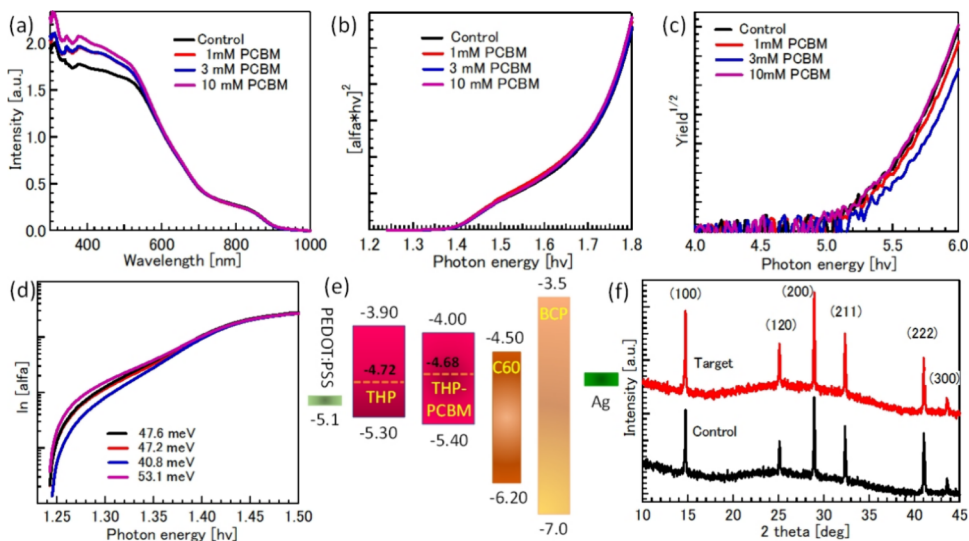


Figure 1. (a) UV–vis absorption spectra of control and PCBM-doped THP films. (b) Tauc plot of control and PCBM-doped THP films. (c) Photoyield spectroscopy of control and PCBM-doped THP films. (d) Urbach energy plot of control and PCBM-doped heterojunction THP films. (e) Energy diagram of the THP-PCBM active layer based fabricated solar cell. (f) XRD pattern of control and target films.

stabilized crystals, reduced trap densities, and suppressed defect states at grains. Concomitantly, surface defect states were effectively managed through the utilization of sulfamic acid.²⁸ Another study involved a CuI–DMSO complex as a dopant, wherein copper filled tin vacancies and iodine-controlled halide deficiency within the bulk perovskite.²⁹ In an alternative approach, a thin layer of thermally deposited Sn metal underwent plasma treatment to form SnO_x. This effectively suppressed interfacial Sn⁴⁺ formation and further improved PCE.^{30,31}

These efforts were focused on controlling the crystallization process to curb Sn defect formation within the bulk or at the interfaces of the THP solar cells. It is important to note that Pb-perovskite solar cells have shown significant advancement in the bulk-heterojunction solar cell fabrication, incorporating n-type [6,6]-phenyl-C61-butyrilic acid methyl ester (PCBM) as an additive.^{32,33} The strategic electronic coupling of PCBM within Pb-perovskite resulted in a hybrid active layer, exhibiting larger grains, minimized hysteresis effect, increased photovoltage, enhanced charge extraction capabilities, and suppressed ion migration. The widespread distribution of PCBM within the bulk perovskite targeted grain boundaries, leading to the passivation of Pb defects. This passivation produced a shallower shift in the Fermi level, ultimately enhancing the photoelectric performance of the solar cells.

THPs are inherently p-type semiconductors and offer excellent hole mobility.² Abate et al. inserted an n-type indacenodithieno-[3,2-*b*]-thiophene interlayer between Sn-perovskite and C60 layers, which effectively enhanced electron transport.³⁴ To effectively harness THP's potential in solar cells, a postsurface treatment involving the Lewis base 6-maleimidohexanehydrazide trifluoroacetate was employed. This treatment transformed the surface nature from p-type to n-type.¹⁴ Furthermore, an edamine treatment coordinated unsaturated bonds, donated electrons, and effectively converted the THP surface from p-type to n-type.³⁵ These surface transformations promote electron transfer and facilitate enhanced PCE. It is important to note that such surface treatment results in a p–n gradient within the film.³⁶ Inspired by these surface transformations, we explore the n-type

electronic properties of PCBM as a dopant within p-type THP solar cells. This strategy involved a blend concept broadly used in organic solar cells. Strategically positioned PCBM at the grain boundaries offers multiple benefits of enhanced adhesion between grains, improved energetic matching at the interfaces, and enhanced charge transfer. The combination of these effects enhanced the photoelectric performance of the THP solar cells.

A simple one-step method utilizing conventional polar solvents DMF and DMSO was chosen to fabricate THP (control) and PCBM-doped THP (target) films. Characterization of PCBM dissolved in a DMF:DMSO solvent mixture followed by film fabrication using the spin coating method was performed. Figure S1 (a) illustrates the UV–vis spectra of PCBM film, displaying a strong peak at 347 nm of the UV region. Additionally, the Tauc plot, PYS spectra, and energy diagram of PCBM film are depicted in Figure S1 (b), S1 (c), and S1 (d). These data showed that PCBM electronic properties are maintained under a DMF:DMSO polar solvent system.³⁷

The UV–vis absorption plot of the THP film with PCBM as an additive exhibited characteristic spectra without any notable shift in onset, maintaining an unchanged band gap energy (Figure 1a, 1b). The electronic structures of the films were characterized using photoyield spectra (PYS) where the valence band maximum (VBM) energy was determined by measuring photoelectron currents corresponding to incident photon energy. The control film exhibited a VBM of −5.30 eV, while the 1, 3, and 10 mM PCBM-based target films displayed VBM values of −5.35 eV, −5.40 eV, and −5.30 eV, respectively (Figure 1c). The 3 mM PCBM-based target film exhibited a deeper conduction band minimum (CBM), calculated following band gap energy values. Such deeper CBM facilitated improved energetic matching at the n-contact, leading to better charge collection. It can be emphasized that PCBM, serving as a dopant, significantly impacts charge transport and collection at the charge selective layers and interfaces. This influence is attributed to the shifted aligned energetic matching levels, indicating a potential collaboration between THP and PCBM. Specifically, the VBM is determined by Sn(5s) and I(5p)

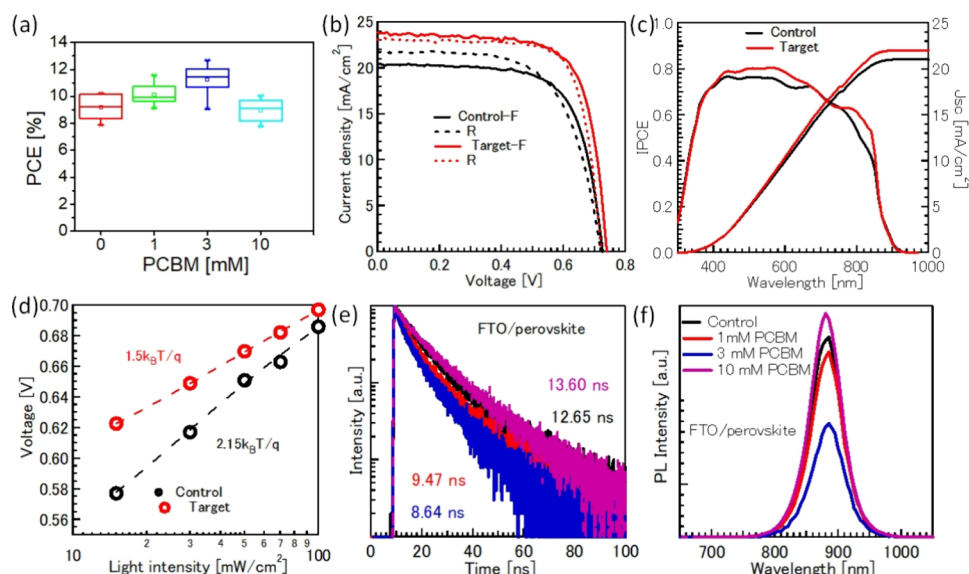


Figure 2. (a) Efficiency box plot of control and PCBM-doped heterojunction solar cells. (b) Champion J – V curves of control and target solar cells. (c) IPCE spectra and calculated J_{sc} of control and champion solar cells. (d) V_{oc} vs light intensity curves of control and target solar cells. (e) TRPL PL spectra of the control film and PCBM-THP heterojunction target films. (f) Steady state PL spectra of control and PCBM-THP heterojunction target films.

antibonding orbitals, while the CBM is determined by I(5p) orbitals.² The degree of energetic disorder of THP films at the band edges within the band gap was analyzed by using Urbach energy (Figure 1d). The Urbach energy values obtained from fitted curves were 47.6 meV, 47.2 meV, 40.8 meV, and 53.1 meV for the control film and 1 mM, 3 mM, and 10 mM PCBM-doped THP films, respectively. The low degree of energetic disorder following PCBM doping indicates reduced trap densities, which will be discussed with DFT results. The energy diagram depicting different layers of fabricated THP solar cells is illustrated in Figure 1e, and the THP layer exhibited a Fermi energy level (E_f) of −4.78 eV, deeper than the mid energy level (E_i) of 4.60 eV, suggesting the p-type semiconducting nature. Upon addition of optimal 3 mM PCBM to the THP, both CBM and VBM shifted to deeper energy states, indicating a reduction in self-doping. Interestingly, E_f shifted to −4.68 eV ≈ E_i (−4.70 eV), indicating the marginal n-type semiconducting nature of the THP layer. Similar behavior of shallower Fermi level has been observed in Pb-perovskite/PCBM heterojunction films.³² Such a modification in semiconducting properties suggests the effective suppression of defect states, resulting in an increased electron concentration.

To assess the influence of PCBM as an additive on the crystal structure properties of THP films, X-ray diffraction (XRD) measurements were conducted (Figure 1f). The obtained characteristic diffraction patterns at $2\theta = 13.97^\circ$, 24.37° , 28.18° , 31.58° , 40.34° , and 42.92° corresponded to the respective crystallographic planes (100), (120), (200), (211), (222), and (300), indicating the orthorhombic pattern of THP films. Notably, the XRD pattern of the PCBM-doped THP film exhibited a similar pattern without any shift, demonstrating the absence of any secondary phase. This confirmed that PCBM predominantly resides on the perovskite film, notably at the grain boundaries, which is similar to Pb-perovskite/PCBM heterojunction solar cells.^{32,33} Furthermore, THP film doped with 3 mM PCBM exhibited a 1.2 times amplified peak, indicating reduced and filling up of grain boundaries. Such

improved crystallization can be explained by the interaction between PCBM and THP, where additional nucleation sites of PCBM retard the crystallization rate. THP semiconducting layers grown by solution-processing methods inevitably form polycrystalline films. In such polycrystalline films, crystal imperfections or grain boundary contacts are the sources of lattice strain. Williamson–Hall analysis is a measure of relative lattice strain component, which is defined as the slope of fit from $\beta \cos \theta = 2 \sin \theta + k\lambda/D$. Here β is full width half-maximum; θ is Bragg angle; λ is the wavelength of X-ray used; k is shape factor; and D is the crystal size. A reduction in strain component observed following PCBM addition suggests a relaxed THP crystal with reduced self-doping pertaining to less exposed grain boundaries and furthers its usefulness in THP perovskite photon-harvesting applications (Figure S2 a). Comparison of Fourier-transform infrared spectra (FTIR) revealed that the stretching vibration of C=O (1735.6 nm) shifted to a lower wavenumber when PCBM was mixed with SnI₂ (Figure S2 b). Such a peak shift suggests the result of an interaction between PCBM and SnI₂.^{38,39} This interaction also implies that PCBM-doped THP had additional nucleation sites, which would suppress the crystallization rates, leading to passivation of undercoordinated Sn²⁺ states at grain boundaries.³⁹ Surface morphology measurements were conducted to confirm the crystal growth phenomenon and grain size estimation (Figure S2 c, S2 d). The grain size of control films was distributed to ≈200 nm. The target heterojunction film had a larger grain size of ≈200–300 nm with relatively homogeneous distribution. This emphasized the reduced grain boundaries in the PCBM-THP film, which is as expected per UV-spectra inspired Tauc plot calculations and XRD measurement results. Atomic force microscopy (AFM) images were conducted to evaluate the effect of PCBM inclusion on the THP films (Figure S2 e, S2 f). The target film showed a flat surface with a low surface roughness ($R_q = 15$ nm) relative to the control film ($R_q = 20$ nm). This further validated the role of PCBM in reducing the surface inhomogeneity, notably arising at the exposed grain boundary contacts and relatively

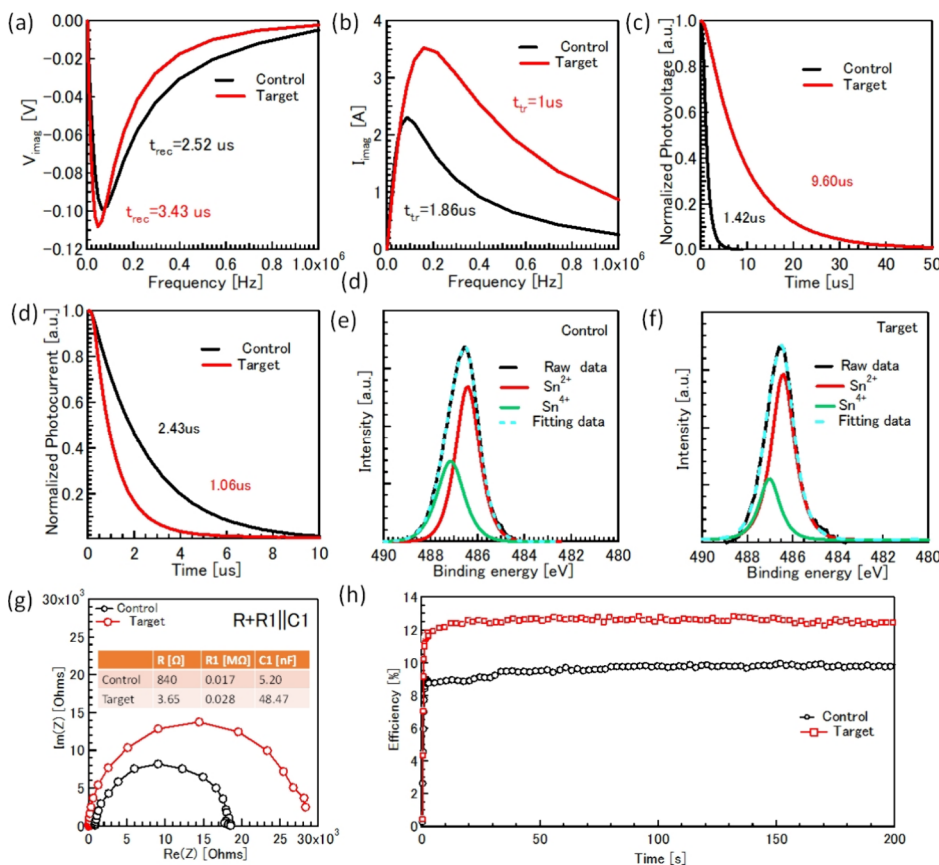


Figure 3. (a) IMVS plot of control and target devices (b) IMPS plot of control and target devices. (c) Transient photovoltage decay curves of control and target devices. (d) Transient photocurrent decay curves of control and target devices. (e) XPS spectra of control film. (f) XPS spectra of target film. (g) Nyquist plot of EIS spectra measured under the dark at open circuit conditions along with fitted electronic parameters. (h) MPPT test measured inside the glovebox.

bigger grain size. Additionally, assessment of the water contact angle (Figure S2 g and h) indicated an enhanced hydrophobic surface behavior of THP film after integration of PCBM, affirming the incorporation of PCBM onto THP films. Improved hydrophobic properties of THP films are supposed to have more repelling behavior toward ambient humidity or water.

The schematic of the solar cell fabrication process is displayed in Figure S3. The JV performance of the solar cells, fabricated in an inverted structure, was assessed under 1 sun condition inside a N_2 -filled glovebox. A box plot of $J-V$ performance exhibiting PCE (Figure 2a), Voc, FF, and Jsc variation is shown in Figure S4. Notably, the PCE values demonstrated an increase with the rise in PCBM additive concentration, a maximum at 3 mM PCBM, beyond which the values declined. This pattern of PCE variation coincides with Jsc and FF, thus explaining the improved charge collection at the interfaces. Figure 2b depicts the best JV characteristics of the solar cells fabricated. The $J-V$ characteristics of a 3 mM PCBM based champion device showed an impressive 12.68% PCE under forward bias (short circuit current (J_{sc}) = 23.85 mA/cm², open circuit voltage (V_{oc}) = 0.73 V, fill factor (FF) = 0.72). Under reverse bias, 12.49% efficiency was obtained (J_{sc} = 23.13 mA/cm², V_{oc} = 0.72 V, FF = 0.75). The control device displayed the best PCE of 10.25% (J_{sc} = 20.47 mA/cm², V_{oc} = 0.72 V, FF = 0.69) in forward bias and 10.07% PCE (J_{sc} = 21.77 mA/cm², V_{oc} = 0.72, FF = 0.64) in reverse bias. Control and target devices showed inverted hysteresis

indexes of 1.75% and 1.50%, respectively. Such inverted hysteresis is presumed to originate under reverse scan due to the screening of electrons by slow mobile I^- ions.⁴⁰ The PCBM residing at the grain boundaries^{32,33} effectively coordinates with these I^- mobile ions, suppressing the hysteresis. The incident photon to collected electron (IPCE) and calculated J_{sc} are represented in Figure 2c. The IPCE spectra notably enlarged in the 780–820 nm range signify increased electron carrier transport and collection. Consequently, an expectation of improved electron collection in the modified THP-PCBM heterojunction film was validated. Furthermore, Voc measurement under varying light intensity provided insights into the recombination dynamics. Figure 2d displays the relationship between the Voc and log plot of light intensity, revealing details about the recombination process. In line with conventional photovoltaic cell equations, $\text{Voc} = (nkT_cq^{-1})\ln(J_{sc}/J_0 + 1)$, where Voc is a function of diode factor (n), Boltzmann constant (k), temperature (T_c), elementary charge (q), and dark current density (J_0). A linear equation depicting the influence of n on light intensity is shown. Since $J_{sc} \gg J_0$ and $J_{sc} \propto$ light intensity, the dependence of light intensity is represented by a linear equation showing the relationship between (nkT_cq^{-1}) and Voc, which dictates the value of n . The value of n becomes unity when recombination loss is absent. A low value of $n = 1.5$ suggests a reduced nonradiative recombination loss in the PCBM-based THP solar cells. The incorporation of PCBM into THP films resulted in notable alterations in photo-

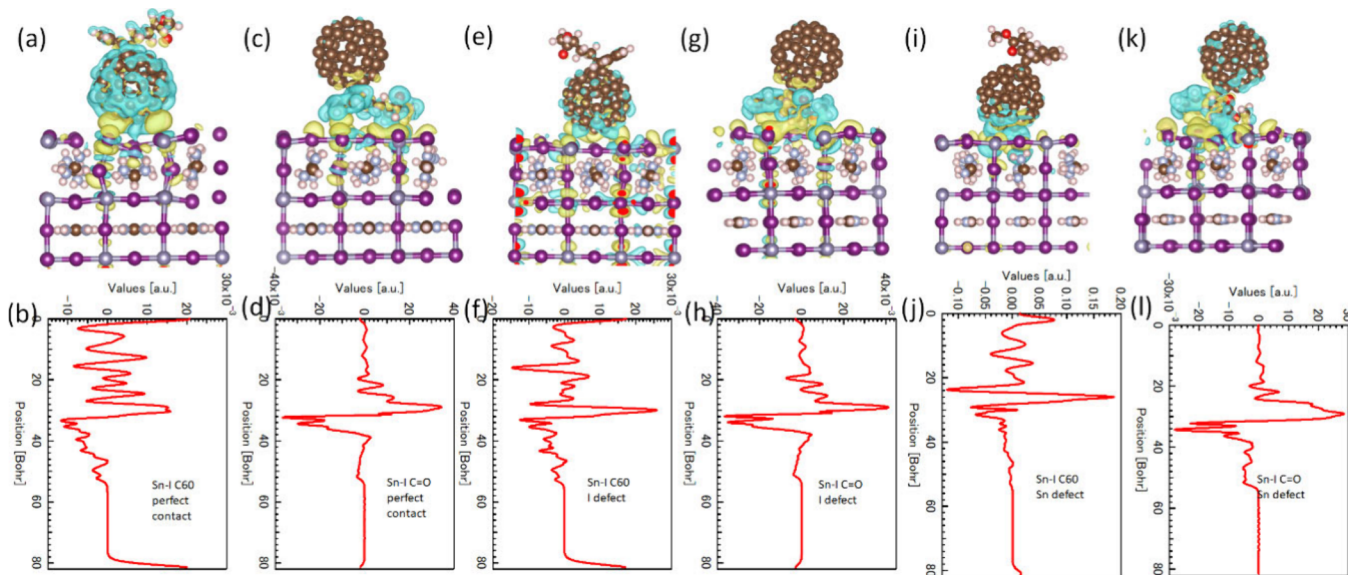


Figure 4. (a) Electronic coupling between C60 and SnI₂ considering a perfect Sn—I surface. (b) Charge interaction between C60 and SnI₂ considering a perfect Sn—I surface. (c) Electronic coupling between O-facing PCBM and the Sn—I surface considering a perfect Sn—I surface. (d) Charge interaction between O-facing PCBM and the Sn—I surface considering the perfect Sn—I surface. (e) Electronic coupling between C60 and the Sn—I surface with I defect states. (f) Charge interaction between C60 and the Sn—I surface with I defect states. (g) Electronic coupling between O-facing PCBM and the Sn—I surface with I defect states. (h) Charge interaction between O-facing PCBM and the Sn—I surface with I defect states. (i) Electronic coupling between C60 and the Sn—I surface having Sn defect states. (j) Charge interaction between C60 and the Sn—I surface having Sn defect states. (k) Electronic coupling between O-facing PCBM and the Sn—I surface having Sn defect states. (l) Charge interaction between O-facing PCBM and the Sn—I surface having Sn defect states.

luminescence (PL) spectroscopy and carrier dynamics as depicted in Figure 2e and 2f. Fabricated on FTO glass, these films underwent PL analysis to calculate the average lifetime through biexponential spectra fitting. τ_1 , τ_2 , A_1 , and A_2 corresponded to faster and slower decay rates, respectively, while A_1 and A_2 represent their respective contributions. THP films doped with 1 and 3 mM PCBM exhibited lower photoluminescence intensity compared to undoped and 10 mM doped films, indicating suppressed defect states and enhanced charge transport efficiency. The time-resolved photoluminescence (TRPL) decay curve indicated a reduced τ_1 value in PCBM-doped films, suggesting that grain boundary trap assisted recombination is mitigated, leading to accelerated charge transport. Additionally, in 1 mM and 3 mM films, a faster τ_2 decay rate suggests suppressed bimolecular radiative electron–hole recombination within the grains, supported by an increased value of the (A_1/A_2) ratio (Table S 1). This highlights that the PCBM sitting at the grain contact suppressed nonradiative recombination within the film near the grain boundary and surface. Conversely, the 10 mM PCBM-THP film displayed an increased faster decay time, τ_2 , likely explaining the diminished PCE observed in such solar cells. Further, the PCBM doping effect on electron transfer rate was evaluated following $A_{\text{PVK}} = (1/\tau_{1\text{PVK/FTO}} - 1/\tau_{1\text{PVK/Glass}})$ and $A_{\text{HeteroPVK}} = (1/(\tau_{1\text{HeteroPVK/FTO}} - 1/\tau_{2\text{PVK/FTO}}))$.⁴¹ A_{PVK} represents the electron transfer rate from the perovskite to the FTO layer, while $A_{\text{HeteroPVK}}$ denotes the electron transfer rate from heterojunction PVK to the FTO layer. The electron transfer rate was 0.94×10^8 s⁻¹ in the pristine perovskite layer. Interestingly, an enhanced electron transfer rate of 2.1×10^8 s⁻¹ was observed in the PCBM-based heterojunction film.

To investigate the charge transport and recombination mechanisms, we conducted intensity-modulated photocurrent spectra (IMPS) and intensity-modulated photovoltage spectra

(IMVS) measurements (Figure 3a, 3b). During IMPS measurement, the solar cell was held at 0 V, while current values were measured. IMPS enables the characterization of charge transport time ($t_{\text{IMPS,tr}}$) defined as $t_{\text{IMPS,tr}} = 1/2\pi f_{\text{IMPS}}$, where f_{peak} represents the intensity at which IMPS reaches its peak.^{42,43} In the PCBM-modified heterojunction THP film as an active layer based solar cell, the $t_{\text{IMPS,tr}}$ decreased from 1.86 to 1 μ s. For the IMVS measurement, the solar cell was maintained at an open circuit voltage, and the voltage was measured upon light illumination to calculate the electron recombination lifetime ($t_{\text{IMVS,rec}}$) defined as $t_{\text{IMVS,rec}} = 1/2\pi f_{\text{IMVS}}$.^{42,43} The fabricated THP solar cell exhibited a $t_{\text{IMVS,rec}}$ of 2.52 μ s, which improved to 3.43 μ s with the THP-PCBM heterojunction film as an active layer. Moreover, the carrier's diffusion constant (D) was determined to support the role of PCBM, calculated using $D = L^2/2.35t_{\text{IMPS,tr}}$.⁴⁴ Additionally, electron diffusion length (L_D) was estimated as $L_D = \sqrt{Dt_{\text{IMVS,rec}}}$. The control film displayed D and L_D values of 9.1×10^{-9} m²/s and 151 nm, respectively, while the PCBM-doped heterojunction THP film demonstrated higher values of 17×10^{-9} m²/s and 241 nm. The increased diffusion constant and electron diffusion length support the reduction in trap density, contributing to the enhanced PCE mainly originating from the better electron movement. Further validation of these results was conducted through transient photovoltage decay (TPV) and transient photocurrent decay (TCV) analyses (Figure 3c, 3d). The fabricated solar cells were operated in open circuit conditions in TPV measurements and under short circuit conditions in TCV measurements.⁴⁵ The charge, recombination time ($t_{\text{TPV,rec}}$), and transport time ($t_{\text{TCV,tr}}$) are defined as the time interval passed during which transport or recombination time decayed to 1/e of the initial values. The observed fitting data align with previous findings, indicating prolonged $t_{\text{TPV,rec}}$ and reduced $t_{\text{TCV,tr}}$ in PCBM clubbed THP

film based solar cells. The control film showed $t_{\text{TPV,rec}} = 1.42 \mu\text{s}$, and it was improved for control devices for $9.60 \mu\text{s}$. $t_{\text{TCV,tr}}$ of target devices was faster ($1.06 \mu\text{s}$) than the control devices ($2.43 \mu\text{s}$). This observation proved the PCBM as an effective dopant for THP films, which reduced the interfacial recombination and defect states.

To elucidate the surface electronic states, X-ray photo-electron spectroscopy (XPS) was carried out. XPS spectra of Sn 3d states elucidated in Figure S5 clearly illustrated that the full width at half-maximum (fwhm) of target film was reduced, validating the previous observation of suppressed defect states amid the interaction between PCBM and THP. The deconvolution of the Sn 3d_{5/2} peak displayed in Figure 3e and 3f showed the relative amount of Sn²⁺ and Sn⁴⁺ species. The ratio of Sn⁴⁺ species in PCBM mixed THP film was suppressed from 36.25% to 24.81%. Hence, XPS observation validated that the PCBM coordination with THP resulted in improved film quality and photovoltaic performance. In the next step, to elucidate the charge-transfer mechanism, electrochemical impedance spectroscopy (EIS) measurements were conducted under dark conditions. Figure 3g presents EIS spectra, which were fitted with an equivalent circuit model, and the inset displays series resistance (R_s), recombination resistance (R_{rec}), and recombination capacitance (C_{μ}). The obtained fitted R_s value for THP-PCBM (3.65Ω) was notably lower than that of THP solar cell (840Ω), elucidating the higher J_{sc} and FF observed in the control solar cell. In comparison to the control solar cell [R_{rec} ($0.017 \text{ M}\Omega$)], the PCBM-THP based solar cell exhibited a higher R_{rec} of $0.028 \text{ M}\Omega$, resulting in a reduced recombination and improved charge collection. Moreover, the PCBM-THP based cell demonstrated an enhanced recombination capacitance of 48.47 nF , significantly improved in contrast to the control solar cell (5.20 nF). A stabilized PCE was observed at the maximum power point measurements inside a N₂ glovebox for 200 s (Figure 3h).

Density functional theory (DFT) has been performed to interpret a possible interaction between PCBM and THP (FASnI₃ (FA = CH(NH₂)₂)) cubic crystals, as shown in Figure 4.^{46,47} The charge difference was calculated to analyze the interaction between PCBM and THP, considering the perfect Sn—I surface, Sn—I surface with V_I, and Sn—I surface with V_{Sn}. Yellow and cyan colors depict regions where electrons are gained and lost. Figure 4a and 4c presents the perfectly optimized configurations for the most suitable attachment of the C60-facing and the O-facing PCBM—tin halide perovskite configuration. Obvious charge transfer is evident in the defect-free perfect contact of PCBM and THP, as depicted in Figure 4b and 4d. This implies a robust interaction between C60 and the C=O group of PCBM with the perfect Sn—I surface. Furthermore, this interaction is anticipated to enhance the interaction of the Sn—I surface, reducing defects/vacancies and preventing the migration of Sn, thereby mitigating the Sn⁴⁺ formation. As reported, THP inherently possesses V_I and V_{Sn}. Considering this, we explore the interaction between PCBM and THP with a vacancy of I, as depicted in Figure 4e, 4f, 4g, and 4h. Notably, in Figure 4e and 4g, significant charge transfer occurs upon PCBM (either C60 or C=O) contact with THP. This outcome indicates that PCBM can effectively passivate iodine defects, leading to an improvement in perovskite quality and an expected reduction in nonradiative recombination. Continuing our valuation, we examined the interaction between THP and PCBM with V_{Sn}, and the results are

illustrated in Figure 4i, 4j, and 4k. In comparison with a perfect Sn—I surface contact, surfaces with Sn vacancies demonstrate a pronounced chemical interaction with PCBM, particularly evident in Figure 4k and 4l. Consequently, PCBM whether C60 or C=O effectively passivates undercoordinated Sn²⁺ sites. The DFT calculations confirm a substantial interaction between PCBM and THP. This theoretical demonstration shows the potential of the PCBM—THP interaction to mitigate THP defects, improving THP quality and reducing non-radiative recombination, an aspect we discussed subsequently.

We have demonstrated that doping of n-type material PCBM into the p-type semiconductor Sn-halide perovskite improves the film quality. The PCBM provided additional nucleation sites and slowed the THP crystallization rate. As a result, the THP-PCBM film exhibited reduced self-doping and intrinsic semiconducting characteristics, facilitating enhanced electron collection. The deeper energetics of the THP film supported easy charge conduction and suppressed charge accumulation. Consequently, we successfully fabricated PCBM—Sn-perovskite heterojunction solar cells with a record 12.68% efficiency.

ASSOCIATED CONTENT

Supporting Information

The Supporting Information is available free of charge at <https://pubs.acs.org/doi/10.1021/acsenergylett.4c01628>.

Experimental details including materials, UV-vis, Tauc plot, PYS spectra, and energy diagram of PCBM thin film with DMF:DMSO (4:1 v/v). Williamson–Hall plot, FTIR spectra, SEM images, AFM images, and water contact angle of THP film and PCBM-THP heterojunction film. Schematics of solar cell fabrication. JV characteristics. Box plot showing FF, J_{sc}, and V_{oc} variations. XPS spectra of Sn 3d (Figures S1–S5). Table S1 lists the PL decay profile data table (PDF)

AUTHOR INFORMATION

Corresponding Authors

Ajay Kumar Baranwal – Info-Powered Energy System Research Center, The University of Electro-Communications, Chofu, Tokyo 182-8585, Japan;  orcid.org/0000-0003-4582-4532; Email: ajaybaranwal@uec.ac.jp

Shuzi Hayase – Info-Powered Energy System Research Center, The University of Electro-Communications, Chofu, Tokyo 182-8585, Japan;  orcid.org/0000-0001-8192-5336; Email: hayase@uec.ac.jp

Authors

Huan Bi – Info-Powered Energy System Research Center, The University of Electro-Communications, Chofu, Tokyo 182-8585, Japan

Gaurav Kapil – Info-Powered Energy System Research Center, The University of Electro-Communications, Chofu, Tokyo 182-8585, Japan

Takeshi Kitamura – Info-Powered Energy System Research Center, The University of Electro-Communications, Chofu, Tokyo 182-8585, Japan;  orcid.org/0009-0005-2782-4549

Liang Wang – Info-Powered Energy System Research Center, The University of Electro-Communications, Chofu, Tokyo 182-8585, Japan

Jiaqi Liu – Info-Powered Energy System Research Center, The University of Electro-Communications, Chofu, Tokyo 182-8585, Japan

Qing Shen – Info-Powered Energy System Research Center, The University of Electro-Communications, Chofu, Tokyo 182-8585, Japan;  orcid.org/0000-0001-8359-3275

Complete contact information is available at:
<https://pubs.acs.org/10.1021/acsenergylett.4c01628>

Author Contributions

#A.K.B. and H.B. contributed equally to this work.

Notes

The authors declare no competing financial interest.

ACKNOWLEDGMENTS

We would like to sincerely thank NEDO.

REFERENCES

- (1) Konstantakou, M.; Stergiopoulos, T. A Critical Review on Tin Halide Perovskite Solar Cells. *J. Mater. Chem. A* **2017**, *5* (23), 11518–11549.
- (2) Baranwal, A. K.; Hayase, S. Recent Advancements in Tin Halide Perovskite-Based Solar Cells and Thermoelectric Devices. *Nanomater.* **2022**, *12* (22), 4055.
- (3) Poli, I.; Kim, G.-W.; Wong, E. L.; Treglia, A.; Folpini, G.; Petrozza, A. High External Photoluminescence Quantum Yield in Tin Halide Perovskite Thin Films. *ACS Energy Lett.* **2021**, *6* (2), 609–611.
- (4) Ighodalo, K. O.; Chen, W.; Liang, Z.; Shi, Y.; Chu, S.; Zhang, Y.; Khan, R.; Zhou, H.; Pan, X.; Ye, J.; Xiao, Z. Negligible Ion Migration in Tin-Based and Tin-Doped Perovskites. *Angew. Chem.* **2023**, DOI: 10.1002/ange.202213932.
- (5) Stoumpos, C. C.; Malliakas, C. D.; Kanatzidis, M. G. Semiconducting Tin and Lead Iodide Perovskites with Organic Cations: Phase Transitions, High Mobilities, and Near-Infrared Photoluminescent Properties. *Inorg. Chem.* **2013**, *52* (15), 9019–9038.
- (6) Noel, N. K.; Stranks, S. D.; Abate, A.; Wehrenfennig, C.; Guarnera, S.; Haghimirad, A.-A.; Sadhanala, A.; Eperon, G. E.; Pathak, S. K.; Johnston, M. B.; Petrozza, A.; Herz, L. M.; Snaith, H. J. Lead-Free Organic-Inorganic Tin Halide Perovskites for Photovoltaic Applications. *Energy Environ. Sci.* **2014**, *7* (9), 3061–3068.
- (7) Baranwal, A. K.; Saini, S.; Sanehira, Y.; Kapil, G.; Kamarudin, M. A.; Ding, C.; Sahamir, S. R.; Yabuki, T.; Iikubo, S.; Shen, Q.; Miyazaki, K.; Hayase, S. Unveiling the Role of the Metal Oxide/Sn Perovskite Interface Leading to Low Efficiency of Sn-Perovskite Solar Cells but Providing High Thermoelectric Properties. *ACS Appl. Energy Mater.* **2022**, *5* (8), 9750–9758.
- (8) Baranwal, A. K.; Saini, S.; Wang, Z.; Hirotani, D.; Yabuki, T.; Iikubo, S.; Miyazaki, K.; Hayase, S. Interface Engineering Using Y_2O_3 Scaffold to Enhance the Thermoelectric Performance of CsSnI_3 Thin Film. *Org. Electron.* **2020**, *76*, 105488.
- (9) Kumar, M. H.; Dharani, S.; Leong, W. L.; Boix, P. P.; Prabhakar, R. R.; Baikie, T.; Shi, C.; Ding, H.; Ramesh, R.; Asta, M.; Graetzel, M.; Mhaisalkar, S. G.; Mathews, N. Lead-Free Halide Perovskite Solar Cells with High Photocurrents Realized through Vacancy Modulation. *Adv. Mater.* **2014**, *26* (41), 7122–7127.
- (10) Zillner, J.; Boyen, H.; Schulz, P.; Hanisch, J.; Gauquelin, N.; Verbeeck, J.; Küffner, J.; Desta, D.; Eisele, L.; Ahlsweide, E.; Powalla, M. The Role of SnF_2 Additive on Interface Formation in All Lead-Free FASnI_3 Perovskite Solar Cells. *Adv. Funct. Mater.* **2022**, *32* (28), 2109649.
- (11) Baranwal, A. K.; Nishimura, K.; Liu, D.; Kamarudin, M. A.; Kapil, G.; Saini, S.; Yabuki, T.; Iikubo, S.; Minemoto, T.; Yoshino, K.; Miyazaki, K.; Shen, Q.; Hayase, S. Relationship between Carrier Density and Precursor Solution Stirring for Lead-Free Tin Halide Perovskite Solar Cells Performance. *ACS Appl. Energy Mater.* **2022**, *5* (4), 4002–4007.
- (12) Nasti, G.; Aldamasy, M. H.; Flatken, M. A.; Musto, P.; Matczak, P.; Dallmann, A.; Hoell, A.; Musiienko, A.; Hempel, H.; Aktas, E.; Di Girolamo, D.; Pascual, J.; Li, G.; Li, M.; Mercaldo, L. V.; Veneri, P. D.; Abate, A. Pyridine Controlled Tin Perovskite Crystallization. *ACS Energy Lett.* **2022**, *7*, 3197–3203.
- (13) Shahbazi, S.; Li, M.-Y.; Fathi, A.; Diau, E. W.-G. Realizing a Cosolvent System for Stable Tin-Based Perovskite Solar Cells Using a Two-Step Deposition Approach. *ACS Energy Lett.* **2020**, *5* (8), 2508–2511.
- (14) Li, H.; Chang, B.; Wang, L.; Wang, Z.; Pan, L.; Wu, Y.; Liu, Z.; Yin, L. Surface Reconstruction for Tin-Based Perovskite Solar Cells. *ACS Energy Lett.* **2022**, *7*, 3889–3899.
- (15) Liao, M.; Yu, B.; Jin, Z.; Chen, W.; Zhu, Y.; Zhang, X.; Yao, W.; Duan, T.; Djerdj, I.; He, Z. Efficient and Stable FASnI_3 Perovskite Solar Cells with Effective Interface Modulation by Low-Dimensional Perovskite Layer. *ChemSusChem* **2019**, *12* (22), 5007–5014.
- (16) Zhang, Z.; Wang, L.; Kumar Baranwal, A.; Razey Sahamir, S.; Kapil, G.; Sanehira, Y.; Akmal Kamarudin, M.; Nishimura, K.; Ding, C.; Liu, D.; Li, Y.; Li, H.; Chen, M.; Shen, Q.; Ripolles, T. S.; Bisquert, J.; Hayase, S. Enhanced Efficiency and Stability in Sn-Based Perovskite Solar Cells by Trimethylsilyl Halide Surface Passivation. *J. Energy Chem.* **2022**, *71*, 604–611.
- (17) Jokar, E.; Chien, C.-H.; Fathi, A.; Rameez, M.; Chang, Y.-H.; Diau, E. W.-G. Slow Surface Passivation and Crystal Relaxation with Additives to Improve Device Performance and Durability for Tin-Based Perovskite Solar Cells. *Energy Environ. Sci.* **2018**, *11* (9), 2353–2362.
- (18) Jokar, E.; Hou, P.; Bhosale, S. S.; Chuang, H.; Narra, S.; Wei-Guang Diau, E. Mixing of Azetidinium in Formamidinium Tin Triiodide Perovskite Solar Cells for Enhanced Photovoltaic Performance and High Stability in Air. *ChemSusChem* **2021**, *14* (20), 4415–4421.
- (19) Nakamura, T.; Yakumaru, S.; Truong, M. A.; Kim, K.; Liu, J.; Hu, S.; Otsuka, K.; Hashimoto, R.; Murdey, R.; Sasamori, T.; Kim, H. Do; Ohkita, H.; Handa, T.; Kanemitsu, Y.; Wakamiya, A. Sn(IV)-Free Tin Perovskite Films Realized by in Situ $\text{Sn}(0)$ Nanoparticle Treatment of the Precursor Solution. *Nat. Commun.* **2020**, *11* (1), 3008.
- (20) Chen, J.; Luo, J.; Hou, E.; Song, P.; Li, Y.; Sun, C.; Feng, W.; Cheng, S.; Zhang, H.; Xie, L.; Tian, C.; Wei, Z. Efficient Tin-Based Perovskite Solar Cells with Trans-Isomeric Fulleropyrrolidine Additives. *Nat. Photonics* **2024**, *18* (5), 464–470.
- (21) Shi, Y.; Zhu, Z.; Miao, D.; Ding, Y.; Mi, Q. Interfacial Dipoles Boost Open-Circuit Voltage of Tin Halide Perovskite Solar Cells. *ACS Energy Lett.* **2024**, *9* (4), 1895–1897.
- (22) Yu, B.; Chen, Z.; Zhu, Y.; Wang, Y.; Han, B.; Chen, G.; Zhang, X.; Du, Z.; He, Z. Heterogeneous 2D/3D Tin-Halides Perovskite Solar Cells with Certified Conversion Efficiency Breaking 14%. *Adv. Mater.* **2021**, *33* (36), 2102055.
- (23) Jokar, E.; Cheng, P.-Y.; Lin, C.-Y.; Narra, S.; Shahbazi, S.; Wei-Guang Diau, E. Enhanced Performance and Stability of 3D/2D Tin Perovskite Solar Cells Fabricated with a Sequential Solution Deposition. *ACS Energy Lett.* **2021**, *6* (2), 485–492.
- (24) Zhao, Z.; Gu, F.; Wang, C.; Zhan, G.; Zheng, N.; Bian, Z.; Liu, Z. Orientation Regulation of Photoactive Layer in Tin-Based Perovskite Solar Cells with Allylammonium Cations. *Sol. RRL* **2020**, *4* (10), 2000315.
- (25) Baranwal, A. K.; Saini, S.; Wang, Z.; Hamada, K.; Hirotani, D.; Nishimura, K.; Kamarudin, M. A.; Kapil, G.; Yabuki, T.; Iikubo, S.; Shen, Q.; Miyazaki, K.; Hayase, S. Effect of Precursor Solution Aging on the Thermoelectric Performance of CsSnI_3 Thin Film. *J. Electron. Mater.* **2020**, *49* (5), 2698–2703.
- (26) Chen, M.; Dong, Q.; Xiao, C.; Zheng, X.; Dai, Z.; Shi, Y.; Luther, J. M.; Padture, N. P. Lead-Free Flexible Perovskite Solar Cells with Interfacial Native Oxide Have > 10% Efficiency and Simultaneously Enhanced Stability and Reliability. *ACS Energy Lett.* **2022**, *7* (7), 2256–2264.

- (27) Kuan, C.-H.; Ko, Y.-A.; Wei-Guang Diau, E. Surface and Interfacial Passivations for FASnI₃ Solar Cells with Co-Cations. *ACS Energy Lett.* **2023**, *8* (5), 2423–2425.
- (28) Kuan, C.-H.; Chih, J.-M.; Chen, Y.-C.; Liu, B.-H.; Wang, C.-H.; Hou, C.-H.; Shyue, J.-J.; Diau, E. W.-G. Additive Engineering with Triple Cations and Bifunctional Sulfamic Acid for Tin Perovskite Solar Cells Attaining a PCE Value of 12.5% without Hysteresis. *ACS Energy Lett.* **2022**, *7* (12), 4436–4442.
- (29) Zhang, Z.; Wang, L.; Bi, H.; Baranwal, A. K.; Kapil, G.; Sanehira, Y.; Liu, J.; Liu, D.; Shen, Q.; Hayase, S. Enhancement of Efficiency and Stability for Tin Halide Perovskite Solar Cells by Using Improved Doping Method. *Adv. Opt. Mater.* **2024**, *12*, 2300962.
- (30) Wang, L.; Miao, Q.; Wang, D.; Chen, M.; Bi, H.; Liu, J.; Baranwal, A. K.; Kapil, G.; Sanehira, Y.; Kitamura, T.; Ma, T.; Zhang, Z.; Shen, Q.; Hayase, S. 14.31% Power Conversion Efficiency of Sn-Based Perovskite Solar Cells via Efficient Reduction of Sn⁴⁺. *Angew. Chem.* **2023**, *62* (33), 1–6.
- (31) Wang, L.; Chen, M.; Yang, S.; Uezono, N.; Miao, Q.; Kapil, G.; Baranwal, A. K.; Sanehira, Y.; Wang, D.; Liu, D.; Ma, T.; Ozawa, K.; Sakurai, T.; Zhang, Z.; Shen, Q.; Hayase, S. SnO_x as Bottom Hole Extraction Layer and Top In Situ Protection Layer Yields over 14% Efficiency in Sn-Based Perovskite Solar Cells. *ACS Energy Lett.* **2022**, *7* (10), 3703–3708.
- (32) Xu, J.; Buin, A.; Ip, A. H.; Li, W.; Voznyy, O.; Comin, R.; Yuan, M.; Jeon, S.; Ning, Z.; McDowell, J. J.; Kanjanaboons, P.; Sun, J.-P.; Lan, X.; Quan, L. N.; Kim, D. H.; Hill, I. G.; Maksymovych, P.; Sargent, E. H. Perovskite–Fullerene Hybrid Materials Suppress Hysteresis in Planar Diodes. *Nat. Commun.* **2015**, *6* (1), 7081.
- (33) Chiang, C.-H.; Wu, C.-G. Bulk Heterojunction Perovskite-PCBM Solar Cells with High Fill Factor. *Nat. Photonics* **2016**, *10* (3), 196–200.
- (34) Zhang, Z.; Su, Z.; Li, G.; Li, J.; Aldamasy, M. H.; Wu, J.; Wang, C.; Li, Z.; Gao, X.; Li, M.; Abate, A. Improved Air Stability of Tin Halide Perovskite Solar Cells by an N-Type Active Moisture Barrier. *Adv. Funct. Mater.* **2024**, DOI: 10.1002/adfm.202306458.
- (35) Kamarudin, M. A.; Hirotani, D.; Wang, Z.; Hamada, K.; Nishimura, K.; Shen, Q.; Toyoda, T.; Iikubo, S.; Minemoto, T.; Yoshino, K.; Hayase, S. Suppression of Charge Carrier Recombination in Lead-Free Tin Halide Perovskite via Lewis Base Post-Treatment. *J. Phys. Chem. Lett.* **2019**, *10* (17), 5277–5283.
- (36) Kapil, G.; Bessho, T.; Maekawa, T.; Baranwal, A. K.; Zhang, Y.; Kamarudin, M. A.; Hirotani, D.; Shen, Q.; Segawa, H.; Hayase, S. Tin-Lead Perovskite Fabricated via Ethylenediamine Interlayer Guides to the Solar Cell Efficiency of 21.74%. *Adv. Energy Mater.* **2021**, *11* (25), 2101069.
- (37) Abdulkarim, Y. I.; Deng, L.; Muhammad, F. F.; He, L. Enhanced Light Absorption in the Organic Thin Films by Coating Cross-Shaped Metamaterial Resonators onto the Active Layers. *Results Phys.* **2019**, *13*, 102338.
- (38) Chen, Y. F.; Luo, Z. M.; Chiang, C. H.; Wu, C. G. Multifunctional Ionic Fullerene Additive for Synergistic Boundary and Defect Healing of Tin Perovskite to Achieve High-Efficiency Solar Cells. *ACS Appl. Mater. Interfaces* **2022**, *14* (41), 46603–46614.
- (39) Ryu, D. H.; Khan, N.; Park, J. G.; Paik, D.; Kang, B. J.; Jeon, N. J.; Lee, S.; Lee, H. K.; Lee, S. K.; Shin, W. S.; Lee, J. C.; Kim, H.; Hong, K. H.; Im, S. H.; Song, C. E. Morphology and Performance Enhancement through the Strong Passivation Effect of Amphoteric Ions in Tin-Based Perovskite Solar Cells. *Small* **2023**, DOI: 10.1002/smll.202302418.
- (40) Richardson, G.; O’Kane, S. E. J.; Niemann, R. G.; Peltola, T. A.; Foster, J. M.; Cameron, P. J.; Walker, A. B. Can Slow-Moving Ions Explain Hysteresis in the Current-Voltage Curves of Perovskite Solar Cells? *Energy Environ. Sci.* **2016**, *9* (4), 1476–1485.
- (41) Chen, M.; Kapil, G.; Li, Y.; Kamarudin, M. A.; Baranwal, A. K.; Nishimura, K.; Sahamir, S. R.; Sanehira, Y.; Li, H.; Ding, C.; Zhang, Z.; Shen, Q.; Hayase, S. Large Synergy Effects of Doping, a Site Substitution, and Surface Passivation in Wide Bandgap Pb-Free ASnI₂Br Perovskite Solar Cells on Efficiency and Stability Enhancement. *J. Power Sources* **2022**, *520*, 230848.
- (42) Pockett, A.; Eperon, G. E.; Peltola, T.; Snaith, H. J.; Walker, A.; Peter, L. M.; Cameron, P. J. Characterization of Planar Lead Halide Perovskite Solar Cells by Impedance Spectroscopy, Open-Circuit Photovoltage Decay, and Intensity-Modulated Photovoltage/Photo-current Spectroscopy. *J. Phys. Chem. C* **2015**, *119* (7), 3456–3465.
- (43) Albadri, A.; Yadav, P.; Alotaibi, M.; Arora, N.; Alyamani, A.; Albrithen, H.; Dar, M. I.; Zakeeruddin, S. M.; Grätzel, M. Unraveling the Impact of Rubidium Incorporation on the Transport-Recombination Mechanisms in Highly Efficient Perovskite Solar Cells by Small-Perturbation Techniques. *J. Physic. Chem. C* **2017**, *121* (45), 24903–24908.
- (44) Aharon, S.; Dymshits, A.; Rotem, A.; Etgar, L. Temperature Dependence of Hole Conductor Free Formamidinium Lead Iodide Perovskite Based Solar Cells. *J. Mater. Chem. A* **2015**, *3* (17), 9171–9178.
- (45) Jiang, T.; Chen, Z.; Chen, X.; Chen, X.; Xu, X.; Liu, T.; Bai, L.; Yang, D.; Di, D.; Sha, W. E. I.; Zhu, H.; Yang, Y. M. Power Conversion Efficiency Enhancement of Low-Bandgap Mixed Pb-Sn Perovskite Solar Cells by Improved Interfacial Charge Transfer. *ACS Energy Lett.* **2019**, *4* (7), 1784–1790.
- (46) Kühne, T. D.; Iannuzzi, M.; Del Ben, M.; Rybkin, V. V.; Seewald, P.; Stein, F.; Laino, T.; Khalilullin, R. Z.; Schütt, O.; Schiffmann, F.; Golze, D.; Wilhelm, J.; Chulkov, S.; Bani-Hashemian, M. H.; Weber, V.; Borštník, U.; Taillefumier, M.; Jakobovits, A. S.; Lazzaro, A.; Pabst, H.; Müller, T.; Schade, R.; Guidon, M.; Andermatt, S.; Holmberg, N.; Schenter, G. K.; Hehn, A.; Bussy, A.; Belleflamme, F.; Tabacchi, G.; Glöß, A.; Lass, M.; Bethune, I.; Mundy, C. J.; Plessl, C.; Watkins, M.; VandeVondele, J.; Krack, M.; Hutter, J. CP2K: An Electronic Structure and Molecular Dynamics Software Package - Quickstep: Efficient and Accurate Electronic Structure Calculations. *J. Chem. Phys.* **2020**, DOI: 10.1063/5.0007045.
- (47) Momma, K.; Izumi, F. VESTA 3 for Three-Dimensional Visualization of Crystal, Volumetric and Morphology Data. *J. Appl. Crystallogr.* **2011**, *44* (6), 1272–1276.